Four-Electron Photochemistry of Dirhodium Fluorophosphine Compounds

Alan F. Heyduk, Ann M. Macintosh, and Daniel G. Nocera*

Contribution from the Department of Chemistry, 6-335, Massachusetts Institute of Technology, 77 Massachusetts Avenue, Cambridge, Massachusetts 02139-4307

Received January 20, 1999. Revised Manuscript Received March 26, 1999

Abstract: The singly bonded dirhodium(II) complex, $Rh_2(dfpma)_3Br_4$ (dfpma = bis(difluorophosphine)-methylamine, $CH_3N(PF_2)_2$), photoreacts when irradiated with UV or visible light. The mixed-valence LRh^0-$Rh^{II}X_2$ species, $Rh_2(dfpma)_3Br_2(L)$, is obtained quantitatively when THF solutions containing $Rh_2(dfpma)_3Br_4$ and excess L = dfpma or PR_3 are photolyzed ($\lambda_{exc} > 436$ nm). The photoreaction quantum yield is $\sim 10^{-2}$ over the near-UV absorption manifold, decreasing slightly as the excitation wavelength is extended into the visible region ($\phi_p^{313-405} = 0.022(3)$, $\phi_p^{436-468} = 0.012(1)$). Continued irradiation with excitation wavelengths coincident with the absorption manifold of the $LRh^0Rh^{II}X_2$ complex results in a second two-electron elimination reaction to give the LRh^0Rh^0L dimer, $Rh_2(dfpma)_3L_2$, again in quantitative yield but with an attenuated quantum efficiency ($\phi_p^{313-365} = 0.0035(3)$, $\phi_p^{405-436} = 0.0017(3)$). For photoreactions performed in THF, the bromine photoproduct is HBr, which may be trapped with 2,6-lutidine. NMR experiments reveal the production of 2 equiv of HBr for each two-electron transformation of the dirhodium photoreagent. The wavelength dependence of ϕ_p and the results of extended Hückel calculations are consistent with the photoreaction occurring from an excited state of dσ* parentage. The ability to preserve the same dσ* electronic structure across the four-electron series allows us to overcome the barriers traditionally associated with metal−halogen bond cleavage and consequently to design a four-electron photoreaction among discrete molecular species.

Introduction

Oxidation−reduction reactions of electronically excited transition metal complexes customarily proceed by one electron. By itself, single-electron transfer is confining inasmuch as most activation reactions involve multielectron processes. Primary one-electron photoredox events must, therefore, be coupled to oxidation−reduction processes remote to the excited state to effect overall multielectron reactivity. This general strategy has largely defined the light-to-energy conversion schemes of the past three decades.[1−6] Such conformity in multielectron design finds its origins in the nature of the excited state, which at the most general level is the same despite the many different types of transition metal photoreagents. As instructive examples, consider the three systems represented in Scheme 1. The photochemistry of mononuclear d^6 metals, for which tris(bipyridyl)ruthenium(II) is the archetype, originates from a metal-to-ligand charge-transfer excited state[7−11] in which electrons localized on the metal and ligand are triplet-paired. One-electron reactions effected at the metal or ligand are conveyed by a relay catalyst to a homogeneous or heterogeneous multielectron site, which is capable of storing the redox equivalents.[1,12−16] A biradical model is also pertinent to the excited-state chemistry of binuclear $d^{7(9)}$ and $d^{8(10)}$ metal complexes, but in different guises. The dσ(or dπ*)dσ* excited states of $d^{7(9)}$−$d^{7(9)}$ complexes are short-lived and dissociative, producing

Scheme 1

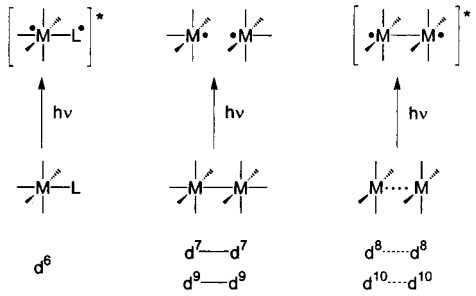

(1) *Photosensitization and Photocatalysis Using Inorganic and Organometallic Compounds*; Kalyanasundaram, K., Grätzel, M., Eds.; Catalysis by Metal Complexes 14; Kluwer Academic: Dordrecht, 1993; pp 247−271.
(2) Amouyal, E. In *Homogeneous Photocatalysis*; Chanon, M., Ed.; Wiley: New York, 1997; pp 263−307.
(3) Bignozzi, C. A.; Schoonover, J. R.; Scandola, F. *Prog. Inorg. Chem.* **1997**, *44*, 1−95.
(4) von Zelewsky, A. *Chimia* **1994**, *48*, 331−335.
(5) Sutin, N.; Creutz, C.; Fujita, E. *Comments Inorg. Chem. A* **1997**, *19*, 67−92.
(6) Roundhill, D. M. *Photochemistry and Photophysics of Metal Complexes*; Plenum Press: New York, 1994.
(7) Schoonover, J. R.; Bignozzi, C. A.; Meyer, T. J. *Coord. Chem. Rev.* **1997**, *165*, 239−266.
(8) Krausz, E.; Ferguson, J. *Prog. Inorg. Chem.* **1989**, *37*, 293−390.
(9) Juris, A.; Balzani, V.; Barigelletti, F.; Campagna, S.; Belser, P.; von Zelewsky, A. *Coord. Chem. Rev.* **1988**, *84*, 85−277.
(10) Kalyanasundaram, K. *Photochemistry of Polypyridine and Porphyrin Complexes*; Academic Press: London, 1982; Chapter 6.
(11) Crosby, G. L. *Acc. Chem. Res.* **1975**, *8*, 231−238.
(12) (a) Argazzi, R.; Bignozzi, C. A.; Hasselmann, G. M.; Meyer, G. J. *Inorg. Chem.* **1998**, *37*, 4533−4537. (b) Garcia, C. G.; Iha, N. Y. M.; Argazzi, R.; Bignozzi, C. A. *J. Photochem. Photobiol. A* **1998**, *115*, 239−242.
(13) Premkumar, J.; Ramaraj, R. *J. Chem. Soc., Dalton Trans.* **1998**, 3667−3672.
(14) Dutta, P. K.; Ledney, M. *Prog. Inorg. Chem.* **1997**, *44*, 209−271.
(15) Levy, B. *J. Electroceram.* **1997**, *1*, 239−272.
(16) Balzani, V.; Barigelletti, F.; Decola, L. *Top. Curr. Chem.* **1990**, *158*, 31−71.

10.1021/ja9902017 CCC: $18.00 © 1999 American Chemical Society
Published on Web 05/15/1999

an •M,M• biradical pair.[17−20] Because the photogenerated radicals are uncoupled, selective multielectron activation of substrates is difficult to control, and therefore free radical reactions are typically observed.[21,22] Conversely, a stable and long-lived biradical tethered by a metal−metal bond, •M−M•, is produced upon the dσ*pσ excitation of $d^{8(10)}$−$d^{8(10)}$ complexes.[23,24] The proximity of the radical metal centers permits coupling of their single-electron reactions to effect selective multielectron transformations.[25,26]

Whereas the general formalism of biradical excited states naturally leads to two-electron processes one electron at a time, approaches to explore photoredox reactions in excess of two electrons are not at hand. In the absence of a well-defined framework, it is not surprising to find scant precedence for three- and four-electron photoreactions. Photoinduced decomposition of Pt^{IV} salts to metal colloids along ill-defined mechanistic pathways is a documented photoredox reaction involving more than two electrons.[27,28] In no case has a four-electron photoreaction along a controlled reaction pathway been achieved.

The challenges confronting the design of multielectron photoreactions are formidable. Reorganization of the primary coordination environment typically accompanies the addition or removal of more than one electron from a metal center. If ligand reorganization does not occur, the thermodynamic barrier associated with the transfer of redox equivalents to or from the metal center becomes insurmountable at chemically relevant redox potentials. This is a particularly germane problem for excited-state redox schemes because reactivity is usually confined to the lowest energy excited state, constraining the overall internal energy of the system. As an example, again consider the oxidation−reduction chemistry of d^6 Ru^{II} polypyridyl systems. The one-electron oxidation and reduction potentials of the Ru^{II} metal, octahedrally coordinated by a conventional polypyridyl ligand set, are ~1.0−1.5 V.[10] By virtue of its inflexibility, the polypyridine coordination sphere imposes thermodynamic remuneration of an additional 1.5 and 3.3 V for the metal-based reduction and oxidation, respectively, of a second electron equivalent.[29] An excited-state energy of only ~2 eV, therefore, confines reaction to single-electron transfer. When the coordination environment of the metal is able to adopt a geometry to accommodate a two-electron photoconversion, the electronic structure responsible for excited-state reactivity is invariably lost.[30] A lowest energy, reactive excited state maintains a fragile existence among the multitude of energy-dissipating excited states of a metal complex. Changes in coordination geometry will reorder state parentages with any one of the neighboring, nonreactive states ready to assume the lowest energy position. In this case, an excited-state pathway encompassing redox reactivity beyond two electrons will be circumvented. With these considerations in mind, we realized that further advances in multielectron photoredox chemistry would require novel molecular structures that would preserve the *same* lowest energy, reactive excited state across a multielectron series of complexes.

Our recent efforts to elaborate conceptually new excited-state complexes that can promote multielectron reactivity have focused on the synthesis of compounds possessing two-electron mixed-valence bimetallic (M^n−M^{n+2}) cores.[31] As single-electron mixed-valence compounds react in one-electron steps from their excited states,[32] electronically excited M^n−M^{n+2} complexes may react in two-electron steps at the bimetallic core. Although the occurrence of authentic M^n−M^{n+2} compounds is unusual,[33−35] we have successfully utilized bis(difluorophosphino)methylamine (dfpma), $CH_3N(PF_2)_2$, to stabilize a Rh^0Rh^{II} core,[36] which is established by the octahedral and trigonal bipyramidal coordination geometries about the Rh^{II} and Rh^0 centers, respectively. The two-electron mixed-valence complex $Rh_2(dfpma)_3X_2(L)$ (L = PF_3 or η^1-dfpma; X = Cl, Br, or I) readily undergoes oxidation and reduction to afford symmetric congeners, $Rh_2(dfpma)_3X_4$ and $Rh_2(dfpma)_3(L)_2$, respectively. Electronic absorption and luminescence spectra of the LRh^0Rh^0L, $LRh^0Rh^{II}X_2$, and $X_2Rh^{II}Rh^{II}X_2$ dfpma complexes are consistent with each possessing a lowest energy excited state of dσ* parentage.[37] We now show that the dσ* excited state allows us to interconvert among LRh^0Rh^0L, $LRh^0Rh^{II}X_2$, and $X_2Rh^{II}Rh^{II}X_2$ cores, enabling us to rationally design a system capable of supporting four-electron photochemistry among discrete molecular species.

Experimental Section

General Considerations. All reactions were performed under the anaerobic conditions provided by standard Schlenk procedures or by the nitrogen atmosphere of a glovebox, capable of supporting a variety of synthetic methodologies. Solvents for synthesis were reagent grade

(17) (a) Vaida, V. In *High Energy Processes in Organometallic Chemistry*; Suslick, K. S., Ed.; ACS Symposium Series 333; American Chemical Society: Washington, DC, 1987; pp 70−80. (b) Rothberg, L. J.; Cooper, N. J.; Peters, K. S.; Vaida, V. *J. Am. Chem. Soc.* **1982**, *104*, 3536−3537.

(18) Zhang, J. Z.; Harris, C. B. *J. Chem. Phys.* **1991**, *95*, 4024−4032.

(19) Owrutsky, J. C.; Baronavski, A. P. *J. Chem. Phys.* **1996**, *105*, 9864−9873.

(20) Kim, S. K.; Pedersen, S.; Zewail, A. H. *Chem. Phys. Lett.* **1995**, *233*, 500−508.

(21) Stufkens, D. J.; van der Graaf, T.; Stor, G. J.; Oskam, A. In *Photoprocesses in Transition Metal Complexes, Biosystems and Other Molecules. Experiment and Theory*; Kochanski, E., Ed.; NATO ASI Series C, Mathematical and Physical Sciences 376; Kluwer Academic: Dordrecht, 1992; pp 217−232.

(22) Geoffrey, G. L.; Wrighton, M. S. *Organometallic Photochemistry*; Academic Press: New York, 1979.

(23) (a) Che, C.-M.; Butler, L. G.; Gray, H. B.; Crooks, R. M.; Woodruff, W. H. *J. Am. Chem. Soc.* **1983**, *105*, 5492−5494. (b) Rice, S. F.; Gray, H. B. *J. Am. Chem. Soc.* **1983**, *105*, 4571−4575. (c) Che, C.-M.; Butler, L. G.; Gray, H. B. *J. Am. Chem. Soc.* **1981**, *103*, 7796−7797.

(24) Fordyce, W. A.; Brummer, J. G.; Crosby, G. A. *J. Am. Chem. Soc.* **1981**, *103*, 7061−7064.

(25) (a) Roundhill, D. M.; Gray, H. B.; Che, C.-M. *Acc. Chem. Res.* **1989**, *22*, 55−61. (b) Smith, D. C.; Gray, H. B. *Coord. Chem. Rev.* **1990**, *100*, 169−181.

(26) (a) Yam, V. W. W.; Lo, K. K. W.; Fung, W. K. M.; Wang, C. R. *Coord. Chem. Rev.* **1998**, *171*, 17−41. (b) Yam, V. W. W.; Choi, S. W. K. *J. Chem. Soc., Dalton Trans.* **1996**, 4227−4232.

(27) Vogler, A.; Quett, C.; Kunkely, H. *Ber. Bunsen. Ges. Phys. Chem.* **1988**, *92*, 1486−1492.

(28) Cameron, R. E.; Bocarsly, A. B. *Inorg. Chem.* **1986**, *25*, 2910−2913.

(29) (a) Tokel-Takvoryan, N. E.; Hemingway, R. E.; Bard, A. J. *J. Am. Chem. Soc.* **1973**, *95*, 6582−6589. (b) Garcia, E.; Kwak, J.; Bard, A. J. *Inorg. Chem.* **1988**, *27*, 4377−4382.

(30) Ying, W.; Pfennig, B. W.; Sharp, S. L.; Ludvig, D. R.; Warren, C. J.; Vicenzi, E. P.; Bocarsly, A. B. *Coord. Chem. Rev.* **1997**, *159*, 245−255.

(31) (a) Nocera, D. G. *Acc. Chem. Res.* **1995**, *28*, 209−217. (b) Nocera, D. G. *J. Cluster Sci.* **1994**, *5*, 185−209.

(32) Vogler, A.; Osman, A. H.; Kunkely, H. *Coord. Chem. Rev.* **1985**, *64*, 159−173.

(33) Young, C. G. *Coord. Chem. Rev.* **1989**, *96*, 89−251.

(34) *Mixed Valency System: Applications in Chemistry, Physics and Biology*; Prassides, K., Ed.; NATO ASI Series C, Mathematical and Physical Sciences 343; Kluwer Academic: Dordrecht, 1991.

(35) Haines, R. J.; Meintjies, E.; Laing, M. *Inorg. Chim. Acta* **1979**, *36*, L403−404.

(36) (a) Dulebohn, J. I.; Ward, D. L.; Nocera, D. G. *J. Am. Chem. Soc.* **1988**, *110*, 4054−4056. (b) Dulebohn, J. I.; Ward, D. L.; Nocera, D. G. *J. Am. Chem. Soc.* **1990**, *112*, 2969−2977.

(37) Kadis, J.; Shin, Y.-g. K.; Dulebohn, J. I.; Ward, D. L.; Nocera, D. G. *Inorg. Chem.* **1996**, *35*, 811−817.

or better, and they were dried by following standard procedures.[38] Spectroscopy and photochemistry experiments employed spectroscopic grade tetrahydrofuran (Burdick & Jackson) and benzene (Aldrich), which were stored over NaK-benzophenone under high vacuum or in a glovebox. All compounds gave satisfactory analyses, which were performed at H. Kolbe Mikroanalytisches Laboratorium.

The preparation of bis(difluorophosphino)methylamine (dfpma) has been reported elsewhere.[39,40] Rhodium starting materials $Rh_2Br_2(C_8H_{12})_2$ and $RhBr[P(C_6H_5)_3]_3$ were prepared according to standard procedures, with the slight modification of utilizing excess LiBr to promote halogen exchange.[41,42] Bromine (Aldrich), phosphorus trifluoride (Elf Atochem), and 2,6-lutidine (Aldrich, redistilled) were used as received, triphenylphosphine (Strem) was recrystallized at least once from hot ethanol, bis(cyclopentadienyl)cobalt(II) (Aldrich) was purified by vacuum sublimation, and 2,3-dimethylbutadiene (Aldrich) was distilled from $NaBH_4$ and stored under high vacuum.

All NMR spectra were collected at the MIT Department of Chemistry Instrumentation Facility (DCIF) on a Varian Unity 300 spectrometer or a Varian Mercury 300 spectrometer in either $CDCl_3$ or C_6D_6 (Cambridge Isotope Laboratories) at 25 °C. ^{1}H (299.871 MHz) and ^{19}F (282.145 MHz) NMR spectra were referenced to the internal standards of TMS and $CFCl_3$, respectively; ^{31}P (121.4 MHz) NMR spectra were referenced to an external 85% H_3PO_4 standard. All chemical shifts are reported using the standard δ notation in parts-per-million; positive chemical shifts are to higher frequency from the given reference.

$Rh_2[CH_3N(PF_2)_2]_3[\eta^1$-$CH_3N(PF_2)_2]L_2$. A 15-mL diethyl ether solution containing 107 mg (0.18 mmol) of $Rh_2Br_2(C_8H_{12})_2$ immediately turned from yellow to red-orange upon the addition of 100 μL (130 mg, 0.78 mmol) of dfpma. Addition of 58 mg of $Co(C_5H_5)_2$ (0.31 mmol) in 15 mL of diethyl ether, followed by stirring for 1 h at room temperature, resulted in the precipitation of cobaltocenium chloride, which was removed by filtration. The filtrate solvent was evaporated in vacuo, and the residue was extracted with 15 mL of pentane. Removal of the pentane by vacuum distillation yielded 126 mg (67%) of the orange product. X-ray quality crystals were obtained by sublimation under high vacuum (10^{-6} Torr) at 120 °C. Anal. Calcd for $C_5H_{15}F_{20}N_5P_{10}Rh_2$: C, 5.77; H, 1.45; N, 6.73; P, 29.76. Found: C, 6.28: H, 1.41; N, 6.77; P, 29.86. ^{19}F NMR (C_6D_6): δ/ppm −29.729 (dd, J^1_{PF} = 1174 Hz, J^3_{PF} = 23.8 Hz, 3.4 F), −40.936 (d, J^1_{PF} = 1116 Hz, 12 F), −76.261 (d, J^1_{PF} = 1252 Hz, 3.8 F). ^{1}H NMR (C_6D_6): δ/ppm 2.29 (s, $\Delta\nu_{1/2}$ = 12.5 Hz, 9 H), 2.44 (s, $\Delta\nu_{1/2}$ = 13.1 Hz, 3 H), 2.47 (s, $\Delta\nu_{1/2}$ = 13.0 Hz, 3 H). ^{31}P NMR ($CDCl_3$): δ/ppm 126−166 (m). ^{31}P(^{19}F) NMR ($CDCl_3$): δ/ppm 139.083 (d, J_{PRh} = 228 Hz), 146.065 (d, J_{PRh} = 198 Hz), 150.810 (bs). Absorption spectrum (THF): λ_{max}/nm (ϵ/M^{-1} cm^{-1}) 310 (24 200), 411 (1170).

$Rh_2[CH_3N(PF_2)_2]_3Br_4$. This binuclear complex was prepared by previously described methods[37] and recrystallized twice from THF and either hexanes or diethyl ether. ^{19}F NMR ($CDCl_3$): δ/ppm −42.534 (bs, $\Delta\nu_{1/2}$ = 94.8 Hz), −44.534 (bs, $\Delta\nu_{1/2}$ = 119.8 Hz), −45.261 (bs, $\Delta\nu_{1/2}$ = 86.7 Hz), −45.19 to −47.09 (m), −49.084 (bs, 134.4 Hz), −49.941 (bs, $\Delta\nu_{1/2}$ = 88.0 Hz), −50.798 (s), −50.941 (s), −57.160 (bs, $\Delta\nu_{1/2}$ = 94.0 Hz), −61.360 (bs, $\Delta\nu_{1/2}$ = 119.9), −71.26 to −72.65 (m), −75.06 to −76.41 (m). ^{31}P NMR ($CDCl_3$): δ/ppm 93−140 (m). ^{1}H NMR ($CDCl_3$): δ/ppm 3.18−3.26 (m). Absorption spectrum (THF): λ_{max}/nm (ϵ/M^{-1} cm^{-1}) 291 (19 600), 400 (12 200), 462 (11 700).

$Rh_2[CH_3N(PF_2)_2]_3Br_2[\eta^1$-$CH_3N(PF_2)_2]$. A 500-mg (0.86 mmol) quantity of $Rh_2Br_2(C_8H_{12})_2$ was suspended in 50 mL of diethyl ether. Addition of 0.4 mL (0.52 g, 3.1 mmol) of dfpma resulted in an immediate color change to dark brown, which lightened to red with the concomitant formation of a precipitate. Reaction was allowed to continue with stirring at room temperature for an additional 2 h. Filtration afforded 608 mg of the red-brown product (68% yield), previously reported[37] but prepared more conveniently and in higher yield as described here. Absorption spectrum (THF): λ_{max}/nm (ϵ/M^{-1} cm^{-1}) 299 (13 900), 358 (11 100), 411 (9510).

$Rh_2[CH_3N(PF_2)_2]_3Br_2[P(C_6H_5)_3]$. A 10-mL benzene solution of $RhBr[P(C_6H_5)_3]_3$ (661 mg, 0.682 mmol) was charged with 124 μL (161 mg, 0.97 mmol) of dfpma. After the solution was stirred at room temperature for 3 h, precipitation of a red solid was induced by the addition of a small volume of pentane. The red-brown powder was collected by filtration and recrystallized twice from methylene chloride and pentane. The yield of the product was 294 mg (76%). X-ray quality crystals were obtained by diffusion of heptane into a saturated methylene chloride solution of the compound. Anal. Calcd for $C_{21}H_{24}Br_2F_{12}N_3P_7Rh_2$: C, 22.34; H, 2.14; N, 3.72. Found: C, 22.25; H, 2.21; N, 3.80. ^{19}F NMR ($CDCl_3$): δ/ppm −33.845 (m), −37.628 (bs, $\Delta\nu_{1/2}$ = 330.2 Hz), −38.421 (bs, $\Delta\nu_{1/2}$ = 90.7), −39.417 (bs, $\Delta\nu_{1/2}$ = 146.4 Hz), −41.471 (bs, $\Delta\nu_{1/2}$ = 108.0 Hz), −42.397 (bs, $\Delta\nu_{1/2}$ = 105.4 Hz), −43.623 (bs, $\Delta\nu_{1/2}$ = 79.2 Hz), −44.742 (s), −47.776 (s), −48.904 (s), −50.061 (bs, $\Delta\nu_{1/2}$ = 93.2 Hz), −51.024 (bs, $\Delta\nu_{1/2}$ = 88.4 Hz), −72.10 (m), −73.34 (m), −75.14 (m), −76.11 (m), −77.29 (m). ^{31}P NMR ($CDCl_3$): δ/ppm 33.772 (bs, $\Delta\nu_{1/2}$ = 202.6 Hz), 11−152 (m).^{1}H NMR ($CDCl_3$): δ/ppm 2.832 (m, 3.0 H), 2.915 (s, 5.9 H), 7.30 to 7.56 (m, 15 H). Absorption spectrum (THF): λ_{max}/nm (ϵ/M^{-1} cm^{-1}) 315 (15 800), 371 (20 400), 424 (22 700).

Synthesis of $Rh_2[CH_3N(PF_2)_2]_3L_2$ (L = Phosphine or Phosphite) Compounds. In a typical synthesis, $Rh_2(dfpma)_3Br_4$ was dissolved in THF. Two equivalents of the desired ligand (L = $P(OCH_3)_3$, $P[OCH(CH_3)_2]_3$, $P(CH_2CH_3)_3$, $P(C_6H_5)_3$) were added to solution, followed by the addition of 4 equiv of $Co(C_5H_5)_2$. The yellow cobaltocenium salt precipitated immediately. The mixture was stirred for several hours and then filtered, and the solvent was removed in vacuo. The resulting residue was extracted with ether, filtered, and dried. Yields varied from 10 to 65%, depending on L.

General Details of X-ray Data Collection and Reduction. X-ray diffraction data were collected on a Siemens diffractometer equipped with a CCD detector. Measurements were carried out at −90 °C using Mo Kα (λ = 0.71073 Å) radiation, which was wavelength selected with a single-crystal graphite monochromator. Four sets of data were collected using ω scans and a −0.3° scan width. All calculations were performed on a Silicon Graphics Indigo 2 workstation. The data frames were integrated to *hkl*/intensity, and final unit cells were calculated by using the SAINT v.4.050 program from Siemens. The structures were solved and refined with the SHELXTL v5.03 suite of programs developed by G. M. Sheldrick and Siemens Industrial Automation, Inc., 1995.

X-ray Structure of $Rh_2[CH_3N(PF_2)_2]_3[\eta^1$-$CH_3N(PF_2)_2]L_2$. A 0.12-mm × 0.12-mm × 0.12-mm orange crystal of block morphology was obtained by sublimation of powder at 120 °C under high vacuum (10^{-6} Torr). The crystal was coated in Paratone N and mounted onto a glass fiber. A total of 12 030 reflections was collected in the θ range of 1.44−23.27°, of which 4354 were unique (R_{int} = 0.0478). The structure was solved by direct methods in conjunction with standard difference Fourier techniques. Hydrogen atoms were placed in calculated positions using a standard riding model and were refined isotropically. The largest peak and hole in the difference map were 0.451 and −0.416 e Å^{-3}, respectively. The least-squares refinement converged normally, giving residuals of R = 0.0649 and wR^2 = 0.1011, and a GOF = 1.124. The crystal data for $C_5H_{15}F_{20}N_5P_{10}Rh_2$ are as follow: monoclinic, *C*2/*c*, *Z* = 8, *a* = 28.3689(14) Å, *b* = 12.4003(6) Å, *c* = 17.3397(9) Å, β = 96.3060(10)°, *V* = 6062.9(5) Å^3, ρ_{calc} = 2.280 g/cm^3, *F*(000) = 4000.

$Rh_2[CH_3N(PF_2)_2]_3Br_2[P(C_6H_5)_3]\cdot 1.5CH_2Cl_2$. A 0.18-mm × 0.18-mm × 0.25-mm maroon crystal of plate morphology, grown by layering a saturated methylene chloride solution with heptane at room temperature, was coated in Paratone N and wax-mounted onto a glass fiber. A total of 8136 reflections was collected in the θ range of 1.56−23.25°, of which 5540 were unique (R_{int} = 0.0376). The structure was solved by direct methods in conjunction with standard difference Fourier techniques. Hydrogen atoms were placed in calculated positions using a standard riding model and were refined isotropically. The solvent atoms of the 1.5 equiv of CH_2Cl_2 in the asymmetric unit were also refined isotropically; the solvent disorder was modeled by standard procedures. The largest peak and hole in the difference map were 2.316 and −1.261 e Å^{-3}, respectively. The least-squares refinement converged

(38) Armarego, W. L. F.; Perrin, D. D. *Purification of Laboratory Chemicals*, 4th ed.; Butterworth-Heinmann: Oxford, 1996.
(39) Nixon, J. F. *J. Chem. Soc. A* **1968**, 2689−2692.
(40) King, R. B.; Gimeno, J. *Inorg. Chem.* **1978**, *17*, 2390−2395.
(41) Osborn, J. A.; Wilkinson, G. *Inorg. Synth.* **1990**, *28*, 77−79.
(42) Giordano, G.; Crabtree, R. H. *Inorg. Synth.* **1990**, *28*, 88−90.

normally, giving residuals of $R = 0.0516$ and $wR^2 = 0.1347$, and a GOF = 1.073. The crystal data for $C_{22.50}H_{24}Br_2Cl_3F_{12}N_3P_7Rh_2$ are as follow: triclinic, $P\bar{1}$, $Z = 2$, $a = 9.289(2)$ Å, $b = 13.159(3)$ Å, $c = 16.937(3)$ Å, $\alpha = 82.23(2)°$, $\beta = 76.31(2)°$, $\gamma = 84.89(2)°$, $V = 1989.6(7)$ Å^3, $\rho_{calc} = 2.092$ g/cm^3, $F(000) = 1208$.

Other Physical Methods. Spectroscopic photolysis measurements were performed on samples contained within a cell equipped with a solvent reservoir and a 1-cm clear fused-quartz cell (Starna Cells, Inc.). The two chambers were isolated from each other by a high-vacuum Teflon valve and from the environment with a second high-vacuum Teflon valve. Bulk photolyses were performed on stirred solutions contained in a quartz reaction vessel adapted for manipulations on a high-vacuum manifold. All photolysis solutions were subject minimally to three freeze−pump−thaw cycles (10^{-6} Torr) prior to irradiation. Samples were irradiated at 0 °C using a 1000-W high-pressure Oriel Hg−Xe lamp. The irradiation beam passed through cutoff filters to remove high-energy light and a collimating lens prior to entering the sample chamber. Quantum yield experiments were performed by replacing the cutoff filters with 10-nm band-pass mercury line interference filters (Oriel). The standard ferrioxalate technique was employed for the calculation of product quantum yields.[43] The progress of a photolysis reaction was monnitored by absorption spectra recorded on an OLIS-modified CARY-17 spectrophotometer.

Identification of the $Rh_2(0,0)$ Product from $Rh_2[CH_3N(PF_2)_2]_3Br_4$/$CH_3N(PF_2)_2$ Photolysis. A 200-mL quartz photolysis tube was charged with 45 mg (44 μmol) of $Rh_2(dfpma)_3Br_4$ in 20 mL of THF under nitrogen. The solution was degassed by three freeze−pump−thaw cycles (10^{-6} Torr), and 0.178 mmol of dfpma was added to the cell under a high-vacuum manifold. The solution was irradiated at 0 °C with 395-nm long-pass filtered light for 46 h. The orange photoproduct was isolated by vacuum distilling solvent from the photolyzed solution, extracting the residue with pentane, and removing solvent in vacuo. ^{19}F NMR (C_6D_6): δ/ppm −29.722 (dd, $J^1_{PF} = 1176$ Hz, $J^3_{PF} = 22.2$ Hz, 3.7 F), −40.957 (d, $J^1_{PF} = 1116$ Hz, 12 F), −76.286 (d, $J^1_{PF} = 1252$ Hz, 3.5 F).

Identification of the Bromine Product Resulting from Rh_2 Dfpma Photochemistry. In the environment of a nitrogen-filled glovebox, 21 mg (20 μmol) of $Rh_2(dfpma)_3Br_4$ was dissolved in 150 mL of THF contained within a quartz photolysis tube. The solution was cooled to −78 °C, and 13 mg (50 μmol) of triphenylphosphine was added, followed by the addition of 10 μL (9.2 mg, 86 μmol) of 2,6-lutidine. The sealed tube was removed from the glovebox, and the solution was irradiated at $\lambda > 335$ nm for 17 h at 0 °C. Solvent was distilled from the photolyzed solution, and the entire residue was dissolved in $CDCl_3$. ^{1}H NMR ($CDCl_3$): δ/ppm 2.60 (bs, 0.96 H), 2.70 (bs, 0.27 H), 2.83 (bs, 0.59 H), 2.91 (bs, 1.18 H), 3.23 (s, 0.09 H), 16.77 (bs, 3.00 H).

Extended Hückel Calculations. Electronic structure calculations were performed on a Silicon Graphics Indy workstation using the YAeHMOP software, v2.0.[44] Valence orbitals for all atoms were used in the basis set. The extended Hückel calculations of the LRh^0Rh^0L and $Br_2Rh^{II}Rh^{II}Br_2$ complexes were performed by using the atomic positions taken from the published crystal structures of $Rh_2(dfpma)_3(PF_3)_2$[36b] and $Rh_2(dfpma)_3Br_4$,[37] respectively. For the mixed-valence compound, an idealized molecule, $Rh_2(dfpma)_3Br_2(PF_3)$, was constructed with the atomic positions obtained from the crystal structure of $Rh_2(dfpma)_3Br_2(\eta^1\text{-dfpma})$. The axially coordinated dfpma ligand was replaced by PF_3 (P−F bond lengths of 1.57 Å and Rh−P−F angles of 120°); bond angles and lengths were obtained from the average values of the terminal PF_3 ligands in the crystal structure of $Rh_2(dfpma)_3(PF_3)_2$. An idealized conformation was adopted such that the PF_3 fluorines were staggered with respect to the three phosphorus atoms of the Rh^0 equatorial plane. The input files for all three molecules are available as Supporting Information. Graphic representations of the metal-based HOMO and LUMO for each molecule were generated from the Viewkel output of the YAeMOP calculation and subsequently modified with the ray-tracing program Rayshade.[45]

Table 1. Selected Bond Distances (Å) and Bond Angles (deg) for $Rh_2(dfpma)_3L_2$ (L = PF_3, η^1-dfpma)

	$Rh_2(dfpma)_3(PF_3)_2$	$Rh_2(dfpma)_3(\eta^1\text{-dfpma})_2$[a]
	Bond Distances	
Rh(1)−Rh(2)	2.841(2)	2.8726(7)
$d(Rh-P_{ax})_{avg}$	2.155	2.191
$d(Rh-P_{eq})_{avg}$	2.219	2.227
	Bond Angles	
Rh(2)−Rh(1)−P(7)	179.4(1)	175.31(6)
Rh(1)−Rh(2)−P(8)	179.5(1)	170.30(5)
P(1)−Rh(1)−P(3)	120.6(2)	115.84(7)
P(5)−Rh(1)−P(3)	116.8(1)	104.84(7)
P(5)−Rh(1)−P(1)	121.2(1)	137.87(7)
P(2)−Rh(2)−P(4)	118.6(2)	106.86(7)
P(6)−Rh(2)−P(2)	119.7(1)	126.10(7)
P(6)−Rh(2)−P(4)	119.9(1)	125.33(7)

[a] Note that the numbering scheme for L = η^1-dfpma is the same as that previously reported for L = PF_3 (ref 36a).

Results and Discussion

Structural Chemistry. The $Rh_2(dfpma)_3L_2$, $Rh_2(dfpma)_3X_2L$, and $Rh_2(dfpma)_3X_4$ complexes constitute a well-defined structural series with octahedral Rh^{II} and trigonal bipyramidal Rh^0 centers composing the binuclear metal core. The hexacoordinate ligand environment of the Rh^{II} center comprises two halide atoms and three phosphorus atoms of the bridging dfpma ligands, with the octahedral coordination sphere completed by the Rh^0 center of the singly bonded Rh_2 core. The coordination environment of the Rh^0 center is defined by an equatorial plane of three phosphorus atoms from the bridging dfpma ligands, axially capped by Rh^{II} and a phosphorus atom from a donor phosphine ligand. We previously established dfpma as an adequate axial donor ligand of the Rh^0 center with the isolation and structural characterization of the bromide complex, $Rh_2(dfpma)_3Br_2(\eta^1\text{-dfpma})$.[37] However, the fully reduced LRh^0-Rh^0L complex has remained conspicuously absent from a complete homologous series featuring η^1-dfpma as a capping ligand. Accordingly, we undertook the preparation and structural characterization of $Rh_2(dfpma)_3(\eta^1\text{-dfpma})_2$.

Though homoleptic complexes of a binuclear Rh^0Rh^0 core are uncommon, with $Rh_2(PF_3)_8$ as a prominent exception,[46] $Rh_2(dfpma)_3(\eta^1\text{-dfpma})_2$ is readily produced from stoichiometric mixtures of $Rh_2Br_2(C_8H_{12})_2$ and dfpma in the presence of mild reductants. Obtained in high yield, the binuclear complex is structurally analogous to its Periodic group counterpart, $Co_2(dfpma)_3(\eta^1\text{-dfpma})_2$.[47] Complete crystallographic details of the structural characterization of $Rh_2(dfpma)_3(\eta^1\text{-dfpma})_2$ are included in the Supporting Information. Table 1 summarizes pertinent geometric parameters of the compound and includes related data for the PF_3 analogue, $Rh_2(dfpma)_3(PF_3)_2$.[36b] The axially coordinated η^1-dfpma and PF_3 consociates are structurally similar. In both compounds, Rh−P bond lengths for the axial phosphine ligands are shorter than those for ligands bridging the metal core. The slightly weaker π-accepting ability of the more electron-rich dfpma ligand, as compared to PF_3, is revealed by an increase of 0.036 Å in the $Rh-P_{ax}$ bond length. The only noteworthy difference between the η^1-dfpma and PF_3

(43) Murov, S. L.; Carmichael, I.; Hug, G. L. *Handbook of Photochemistry*, 2nd ed.; Marcel Dekker: New York, 1993.

(44) Landrum, G. A. *YAeHMOP: Yet Another extended Hückel Molecular Orbital Package*. YAeHMOP is freely available on the World Wide Web at http://overlap.chem.cornell.edu:8080/yaehmop.html.

(45) Kolb, C.; Bogart, R.; *Rayshade*, v. 4.0. Rayshade is available on the World Wide Web at http://aperture.stanford.edu/~cek/rayshade/rayshade.html.

(46) Bennett, M. A.; Patimore, D. J. *Inorg. Chem.* **1971**, *10*, 2387−2395.

(47) King, R. B.; Gimeno, J.; Lotz, T. J. *Inorg. Chem.* **1978**, *17*, 2401−2405.

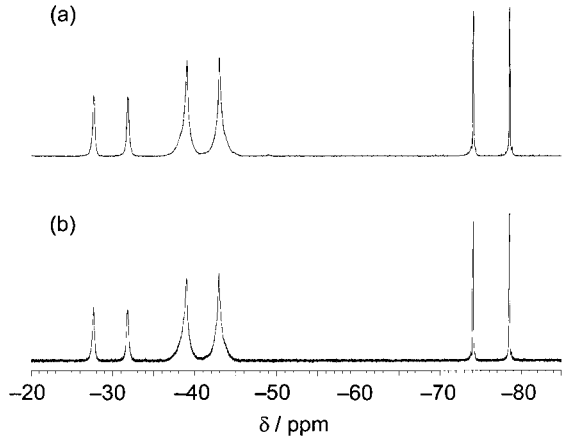

Figure 1. (a) ^{19}F NMR spectrum of $Rh_2(dfpma)_3(\eta^1\text{-dfpma})_2$ in C_6D_6. (b) ^{19}F NMR (C_6D_6) spectrum of the photoproduct obtained from the irradiation ($\lambda_{exc} > 335$ nm) of $Rh_2(dfpma)_3Br_4$ in the presence of excess dfpma in THF at 0 °C (see later discussion). The photoproduct was isolated by removal of THF in vacuo and extraction with pentane.

structures arises from the greater degrees of freedom accompanying the dangling dfpma ligand. In the solid state, the free ends of both capping ligands curl in the same direction, leading to a distortion from the D_3 symmetry of the PF_3-capped compound.

The distinct coordination environments of the two types of dfpma ligands in $Rh_2(dfpma)_3(\eta^1\text{-dfpma})_2$ are evident in the ^{19}F NMR spectrum, which is reproduced in Figure 1a. The presence of only three doublet signals is consistent with three unique fluorine environments under D_3 symmetry for the bridged dfpma, and for the axially coordinated and uncoordinated ends of η^1-dfpma. The 1:3:1 integration pattern for the −29.73, −40.94, and −76.26 ppm resonances (relative to $CFCl_3$) unambiguously leads to an assignment of the −40.94 ppm resonance to the fluorines of the bridging ligands. Of the two remaining resonances, the pronounced high-frequency shift of the −29.73 ppm resonance distinguishes the fluorines of the coordinated phosphorus of the axial η^1-dfpma from those at the uncoordinated end of the ligand. Assignment of the −76.26 ppm resonance to the fluorines of the dangling end of the η^1-dfpma ligand is further supported by the ^{19}F NMR spectrum of free dfpma, which exhibits a doublet centered at −75 ppm.

Although ^{31}P NMR might be expected to be a useful structural probe of the dirhodium coordination environment, spectral congestion arises from coupling constants that are large compared to the differences in chemical shift values. The ^{31}P NMR spectrum shows several overlapping signals in the 126−166 ppm range, with no discernible improvement in resolution over a temperature range of −70 to +80 °C. Straightforward spectra are obtained, however, when ^{19}F decoupling is employed. The $^{31}P\{^{19}F\}$ NMR spectrum exhibits three unique ^{31}P resonances at 150.8, 146.1, and 139.1 ppm relative to H_3PO_4. P−Rh coupling identifies the high-frequency resonances as originating from bridging (146.1 ppm, $J_{P-Rh} = 198$ Hz) and axially coordinated (139.1 ppm, $J_{P-Rh} = 228$ Hz) fluorophosphines. The assignment of P_{ax} to the lower frequency resonance (139.1 as compared to 146.1 ppm) is based on the expected shift that is induced by coordination along the electron-rich metal−metal bond. The uncoordinated phosphorus of the η^1-dfpma gives a broad singlet at 150.8 ppm.

The $Rh_2(dfpma)_3(\eta^1\text{-dfpma})_2$ compound is stable toward air oxidation, but moisture leads to facile hydrolysis of the uncoordinated ends of the η^1-dfpma ligands, to afford $Rh_2(dfpma)_3[PF_2NH(CH_3)]_2$. The loss of the −76.26 ppm resonance in the ^{19}F NMR spectrum and the appearance of resonances at −31.8 and −39.9 ppm for the axial PF_2NHCH_3 and bridging dfpma ligands, respectively, are signatures of the hydrolysis reaction. Introduction of PR_3 at the Rh^0 center(s) in $LRh^0Rh^{II}Br_2$ and LRh^0Rh^0L simplifies the chemistry of the system by removing the hydrolytic instability of the axial ligand. Whereas the direct substitution reaction of η^1-dfpma by PR_3 proceeds sluggishly, $Rh_2(dfpma)_3(PR_3)_2$ is cleanly produced from the reduction of $Rh_2(dfpma)_3Br_4$ in the presence of the desired ligand at room temperature. Because it is difficult to cleanly terminate reduction of the $X_2Rh^{II}Rh^{II}X_2$ core at two electrons, even when mild reductants are employed, the $Rh_2(dfpma)_3Br_2(PR_3)$ compounds are most easily prepared from the disproportionation of the Rh^I complexes, $RhBr(PR_3)_3$ or $Rh_2Br_2(PR_3)_4$, in the presence of $CH_3N(PF_2)_2$.

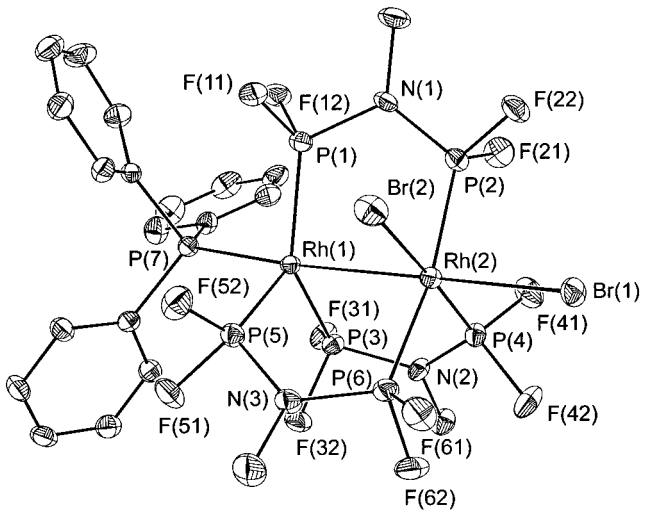

Figure 2. ORTEP view of the crystal structure of $Rh_2(dfpma)_3Br_2(PPh_3)\cdot 1.5CH_2Cl_2$. Thermal ellipsoids are drawn at the 35% probability level, and the numbering scheme is shown. Solvent molecules are omitted for clarity.

Table 2. Selected Bond Lengths (Å) and Distances (deg) for the Metal Core of $Rh_2(dfpma)_3Br_2[P(C_6H_5)_3]$

$N-P^{Rh(II)}$		$N-P^{Rh(0)}$	
N−P Bond Distances (Bridging dfpma Ligands)			
N(1)−P(2)	1.630(6)	N(1)−P(1)	1.684(5)
N(2)−P(4)	1.634(6)	N(2)−P(3)	1.684(5)
N(3)−P(6)	1.636(6)	N(3)−P(5)	1.685(6)
Bond Distances			
Rh(1)−Rh(2)	2.8383(9)	Rh(2)−Br(1)	2.6066(10)
Rh(1)−P(7)	2.335(2)	Rh(2)−Br(2)	2.5020(11)
Rh(1)−P(1)	2.238(2)	Rh(2)−P(2)	2.254(2)
Rh(1)−P(3)	2.202(2)	Rh(2)−P(4)	2.184(2)
Rh(1)−P(5)	2.259(2)	Rh(2)−P(6)	2.249(2)
Bond Angles			
Rh(2)−Rh(1)−P(7)	175.26(5)	Br(2)−Rh(2)−P(4)	177.26(5)
Rh(1)−Rh(2)−Br(1)	179.01(3)	Br(2)−Rh(2)−P(6)	83.46(5)
Rh(1)−Rh(2)−Br(2)	89.38(3)	P(1)−Rh(1)−P(3)	137.10(7)
Br(2)−Rh(2)−P(2)	85.96(5)	P(1)−Rh(1)−P(5)	118.33(7)

The isolation and characterization of the $Rh_2(dfpma)_3Br_2(PR_3)$ complexes has provided us with insights into the mechanism by which the two-electron mixed-valence core is stabilized. Figure 2 displays the high-resolution X-ray crystal structure of $Rh_2(dfpma)_3Br_2(PPh_3)$. Bond length differences, which lie well outside 3 esd for this X-ray structure (esd = 0.006 Å), reveal a pronounced asymmetry in the bridging dfpma ligand framework (Table 2). The N−P bonds adjacent to the $P-Rh^{II}$ are 0.05 Å shorter than those adjacent to the $P-Rh^0$ (average

N−$P^{Rh(II)}$ = 1.633(6) Å, average N−$P^{Rh(0)}$ = 1.684(5) Å). Lone pair donation from N to the PF_2 bonded to Rh^{II} provides sufficient electron density to the fluorophosphine that minimal π-back-bonding from the metal is required, thus leading to a stable $Rh^{II}-PF_2$ bond. With the N lone pair electron density channeled away from the PF_2 groups bonded to the Rh^0, the strong dπ accepting properties of the other PF_2 group are maintained, and hence the Rh^0 is stabilized. In this manner, we believe that the $CH_3N(PF_2)_2$ ligand is able to promote the intramolecular disproportionation of Rh^IRh^I to $Rh^{II}Rh^0$.

Table 2 also lists selected metrical parameters about the dirhodium core. Along the metal−metal axis, all bonds are elongated relative to the analogous η^1-dfpma compound (d(Rh−P_{ax}) = 2.203(6) Å and d(Rh−Rh) = 2.798(2) Å for Rh_2(dfpma)$_3$-Br_2(η^1-dfpma)[37]). The significantly longer Rh−P_{ax} bond length of the PPh_3 complex (Δd = 0.132 Å) is attributed to the poor π-accepting properties of PPh_3 as compared to dfpma, which is generally considered an efficacious π-accepting ligand.[48] The metal−metal bond length appears to be dominated by stereoelectronic effects within the σ-framework, a situation that is typical for bimetallic complexes. The stronger Lewis base character of PPh_3 as compared to dfpma will result in greater Lσ−dσ orbital mixing, which in turn will destabilize the dσ level and increase the Rh−Rh bond distance (Δd = 0.040 Å). The steric bulk of the PPh_3 further perturbs the dirhodium bond distance. The crystal structure of the Rh_2(dfpma)$_3Br_2$(PPh_3) reveals that the Rh^0 center lies toward the P_{ax} atom, 0.111 Å above the basal plane defined by the three equatorial P atoms of the bridging dfpma ligands. This out-of-plane distortion is 0.035 Å greater than that observed in the η^1-dfpma compound. A commensurate increase in the Rh−Rh distance of 0.040 Å shows that the Rh−P_{ax} structural subunit is pushed away from the neighboring Rh^{II} metal center, a result of the repulsion between the phenyl substituents of the bulky PPh_3 and the fluorines of the bridging dfpma ligands. For the Rh_2(dfpma)$_3L_2$ complexes, this steric congestion between the PPh_3 and dfpma ligands is manifested at both axial sites, the consequences of which are revealed in the compounds' syntheses. Yields of Rh_2-(dfpma)$_3$(PR_3)$_2$ (PR_3 = P(OMe$_3$)$_3$, P[OCH(CH$_3$)$_2$]$_3$, PEt$_3$, PPh_3) are lowest for PPh_3, which exhibits the largest cone angle in this group of phosphines. For phosphines exhibiting cone angles larger than that of PPh_3, such as P(C_6F_5)$_3$ (cone angle of 184°), the Rh_2(dfpma)$_3$(PR_3)$_2$ complex could not be isolated.

Electronic Spectroscopy. The electronic absorption spectra displayed in Figure 3 clearly distinguish the members of the Rh_2(dfpma)$_3Br_4$, Rh_2(dfpma)$_3Br_2$(η^1-dfpma), and Rh_2(dfpma)$_3$-(η^1-dfpma)$_2$ series. The high optical electronegativity of the terminal fluorophosphine ligand reduces configurational mixing[49] of the dσ and Lσ orbitals, and a relatively straightforward absorption spectrum, typical of d^9-d^9 compounds,[6,22,50] is observed for Rh_2(dfpma)$_3$(η^1-dfpma)$_2$. An intense 310-nm band, attributable to the allowed dσ → dσ* transition, is flanked to lower energy by the less intense dπ* → dσ* absorption band. Comparison of the energy maxima of these absorption bands to those previously observed for the PF_3 complex[37] indicates that η^1-dfpma substitution does little to perturb the electronic environment of the LRh^0Rh^0L core. The absorption spectra of Rh_2(dfpma)$_3Br_4$ and Rh_2(dfpma)$_3Br_2$(η^1-dfpma) exhibit more congested profiles in the near-UV as a result of configurational mixing between the metal d_{z^2} and Br pσ orbitals. Significant LMCT character of the higher energy absorption bands is revealed by their red shift of 3500 and 7600 cm^{-1} upon substitution of chloride by bromide and bromide by iodide, respectively. The low-energy absorption band red shifts to a lesser extent along the same halide series (825 cm^{-1} for Cl$^-$/Br$^-$ and 3600 cm^{-1} for Br$^-$/I$^-$), consistent with greater metal-based character of a dπ* → dσ* transition.[37] Coordinating solvents do not affect the electronic structure of the compounds, as evidenced by the similarity between the absorption spectra obtained for compounds dissolved in CH_2Cl_2 and THF.

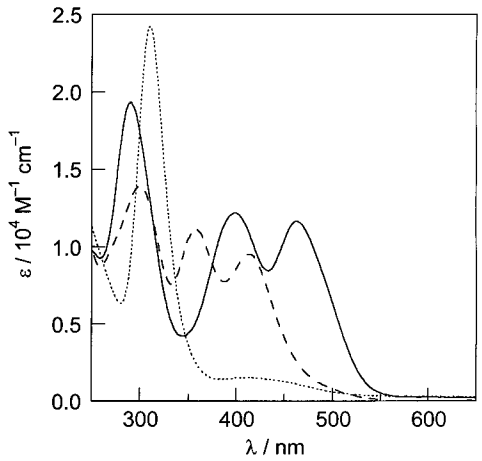

Figure 3. Electronic absorption spectra of Rh_2(dfpma)$_3Br_4$ (—), Rh_2(dfpma)$_3Br_2$(η^1-dfpma) (− − −), and Rh_2(dfpma)$_3$(η^1-dfpma)$_2$ (•••) in THF at room temperature.

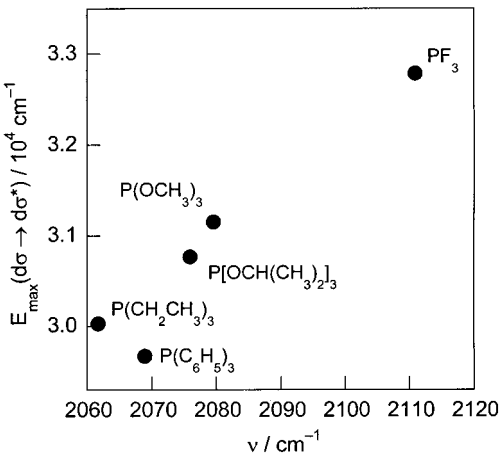

Figure 4. Plot of the energy maximum of the dσ → dσ* transition of Rh_2(dfpma)$_3L_2$ (L = P(CH_2CH_3)$_3$, P(OCH_3)$_3$, P[OCH(CH_3)$_2$]$_3$, P(C_6H_5)$_3$, and PF_3) vs Tolman's electronic parameter.

Whereas substitution of PF_3 by η^1-dfpma is electronically mundane, coordination of the more basic PR_3 ligands to the Rh^0 center of the Rh_2 dfpma series notably perturbs the electronic structure of the system. Consistent with the elongated Rh−Rh bond distance of Rh_2(dfpma)$_3Br_2$(PPh_3), absorption maxima of this complex are significantly red-shifted (>20 nm) (see Experimental Section for detailed listings) to those of LRh^0-$Rh^{II}Br_2$ complexes featuring fluorophosphine as the axial ligand. The effect is even more pronounced in the absorption spectra of the diaxially substituted LRh^0Rh^0L compounds. Figure 4 plots the absorption maximum of the dσ → dσ* transition of Rh_2-(dfpma)$_3L_2$ for L = P(CH_2CH_3)$_3$, P(OCH_3)$_3$, P[OCH(CH_3)$_2$]$_3$, PPh_3, and PF_3 vs the Tolman electronic parametrization of phosphine ligands.[51] The observed trend of the dσ → dσ* transition toward lower energy with an increase in the basicity

(48) King, R. B. *Acc. Chem. Res.* **1980**, *13*, 243−248.

(49) (a) Miskowski, V. M.; Gray, H. B. In *Understanding Molecular Properties*; Avery, J., Dahl, J. P., Hansen, A. E., Eds.; Reidel: Dordrecht, 1987; p 1. (b) Miskowski, V. M.; Smith, T. P.; Loehr, T. M.; Gray, H. B. *J. Am. Chem. Soc.* **1985**, *107*, 7925−7934.

(50) Reinking, M. K.; Kullburg, M. L.; Cutler, A. R.; Kubiak, C. P. *J. Am. Chem. Soc.* **1985**, *107*, 3517−3524.

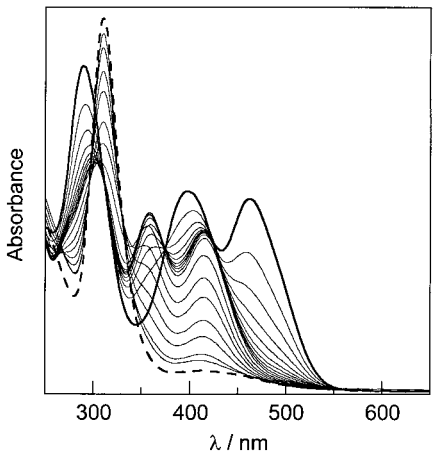

Figure 5. Changes in the electronic absorption spectrum during the photolysis (λ_{exc} > 335 nm) of $Rh_2(dfpma)_3Br_4$ in THF and in the presence of 250 equiv of dfpma at 0 °C. Spectra were recorded over the span of 2 h (initial (—), final (– – –)).

of the phosphine logically follows from considerations of Pσ orbital mixing into the metal−metal σ framework. Although linear combinations of Pσ orbitals have the appropriate symmetries to mix with both dσ and dσ*, destabilization of the energetically more proximate dσ orbital will be greater, resulting in the observed red shift. With the exception of PPh_3, the size of the phosphine is of little consequence in the overall correlation since the cone angles of the phosphines are relatively constricted (<135°). We attribute the anomalously small dσ → dσ* transition energy of PPh_3 to structural distortions of the ligand and metal framework of the type observed in the crystal structure of the $Rh_2(dfpma)_3Br_2(PPh_3)$. The steric-induced lengthening of the Rh−Rh bond by PPh_3 augments the ligand's electronic effect, leading to a smaller dσ/dσ* splitting and consequently a lower observed transition energy than that predicted by the Tolman electronic parameter.

Excitation into the absorption manifold of crystalline solids of the Rh_2 dfpma compounds produces a long-lived red luminescence with spectral features characteristic of a dσ*-state parentage.[52,53] Luminescence is not detected from solutions at temperatures equivalent to those at which the crystalline solids emit. Moreover, the loss of luminescence from solutions of the Rh_2 dfpma complexes immediately above solvent glassing transition temperatures suggested to us the prevalence of bond cleavage chemistry as a dominant nonradiative decay pathway of the dσ* excited state. These photophysical observations provided us with the impetus to undertake investigations of the solution photochemistry of this series of complexes.

Photochemistry. Figure 5 conveys the complexity of $Rh_2(dfpma)_3Br_4$ photochemistry when THF solutions of the compound are photolyzed at λ_{exc} > 335 nm.[54] Isosbestic points at 311, 373, and 425 nm, maintained early during photolysis, are lost with continued irradiation, indicating the occurrence of a secondary reaction at longer times. Comparison of the terminating absorption profile of the photolyzed solution to the absorption spectra in Figure 3 identifies the final photoproduct as $Rh_2(dfpma)_3(\eta^1\text{-dfpma})_2$, which is confirmed by the data

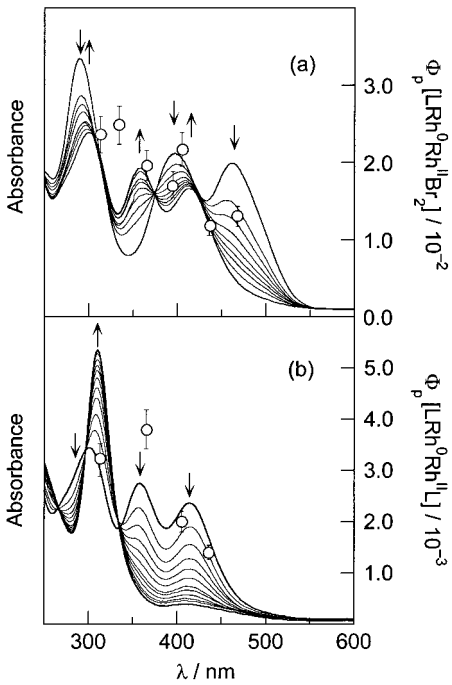

Figure 6. (a) Changes in the electronic absorption spectrum during the photolysis (λ_{exc} > 436 nm) of $Rh_2(dfpma)_3Br_4$ in THF and in the presence of 250 equiv of dfpma at 0 °C. Spectra were recorded over the span of 15 min; the photolysis was terminated when the 358-nm absorption was maximized. (b) Spectral changes associated with continued irradiation of solution (a) with higher energy light (λ_{exc} > 335 nm). Spectra were recorded over the span of 3 h. The open circles in spectra (a) and (b) are the product appearance quantum yields (ϕ_p) measured under conditions identical to those used for the photolysis experiments. Error limits were determined from three measurements of the quantum yield at a given wavelength.

reproduced in Figure 1b. The ^{19}F NMR spectrum of the solid isolated from bulk photolyzed solutions is identical to that of independently prepared $Rh_2(dfpma)_3(\eta^1\text{-dfpma})_2$.

Wavelength selection of the excitation light allows us to deconstruct the overall phototransformation of Figure 5 into a stepwise reaction sequence. Figure 6a displays the changes in the absorption profile when a THF solution of $Rh_2(dfpma)_3Br_4$ is photolyzed at λ_{exc} > 436 nm. Well-anchored isosbestic points are maintained throughout the photolysis. Comparison of the terminating absorption spectrum to those of Figure 3 reveals that $Rh_2(dfpma)_3Br_2(\eta^1\text{-dfpma})$ is the photoproduct. On the basis of the measured molar absorption coefficients, the photoconversion of the $Br_2Rh^{II}Rh^{II}Br_2$ complex to the mixed-valence $LRh^0Rh^{II}Br_2$ complex is quantitative. Although this photoreacted solution is stable under the low-energy excitation conditions of Figure 6a, further reaction is observed when the excitation wavelength is moved into the UV spectral region. As shown in Figure 6b, the final absorption spectrum of the solution under 335-nm irradiation is that of $Rh_2(dfpma)_3(\eta^1\text{-dfpma})_2$, which is also produced in quantitative yield. These results demonstrate that the overall photoreaction proceeds in two steps: $Rh_2(dfpma)_3Br_4$ is photolyzed to $Rh_2(dfpma)_3Br_2(\eta^1\text{-dfpma})$ for λ_{exc} > 436 nm and subsequently $Rh_2(dfpma)_3Br_2(\eta^1\text{-dfpma})$ is photolyzed to $Rh_2(dfpma)_3(\eta^1\text{-dfpma})_2$ for λ_{exc} > 335 nm.

The fate of Br in the overall photoreaction sequence is disclosed by undertaking the appropriate trapping experiments. Because the weak C_α−H bonds of THF are susceptible to hydrogen atom abstraction,[55] we suspected that THF might trap the primary Br photoproduct. Two observations support this contention. No photoreaction is observed in benzene or CH_2-

(51) Tolman, C. A. *Chem. Rev.* **1977**, *77*, 313−48.
(52) Shin, Y.-g. K.; Miskowski, V. M.; Nocera, D. G. *Inorg. Chem.* **1990**, *29*, 2308−2313.
(53) Kunkely, H.; Vogler, A. *J. Organomet. Chem.* **1997**, *541*, 177−179.
(54) Under the same conditions used for photolysis, THF solutions of $Rh_2(dfpma)_3Br_4$ are indefinitely stable. As solutions are warmed (T > 40 °C), however, a thermal reaction occurs over the course of several days to yield an unidentified product (λ_{max} = 352 nm).

Cl_2 unless a Br trap such as 2,3-dimethyl-1,3-butadiene (DMB) is present. The inability of these solvents to furnish a hydrogen atom appears to circumvent net photochemistry, as the Br photoproduct can simply recombine with the metal in the absence of DMB. Conversely, photoreactions in THF proceed with facility regardless of the concentration of auxiliary trapping reagent. Addition of DMB to THF solutions of $Rh_2(dfpma)_3Br_4$ or $Rh_2(dfpma)_3Br_2(\eta^1\text{-dfpma})$ has little effect on the overall conversion efficiency (e.g., the quantum yield of $Rh_2(dfpma)_3Br_2(\eta^1\text{-dfpma})$ photolysis in the absence and in the presence of DMB (0.1 M) is $\phi_p^{366} = 5.8 \times 10^{-4}$ and 4.8×10^{-4}, respectively). Considering the high concentration of neat solvent, DMB cannot effectively compete for the Br photoproduct, and thus its presence has little effect on the outcome of the photochemistry performed THF.

If hydrogen atom abstraction from THF does occur, the ultimate fate of the Br photoproduct should be HBr. The conditions under which the above photolysis reactions were executed, however, precluded HBr detection. Because hydrohalic acids readily hydrolyze the N−P bond of F_2PNR_2 to form $[H_2NR_2]^+X^-$ (and PF_2X),[56] we realized that HBr would be scavenged by the excess dfpma present under photolytic conditions, thus preventing its stoichiometric determination. Accordingly, we sought to replace dfpma with a ligand capable of coordinating Rh^0 but incapable of hydrolysis. While any number of PR_3 ligands meet these functional criteria, we settled on PPh_3 as a result of our familiarity with the structure and spectroscopy of this system.

The photochemistry of $Rh_2(dfpma)_3Br_4$ in the presence of excess PPh_3 proceeds according to the same two-step reaction sequence that was described for dfpma, with the minor difficulty that $Rh_2(dfpma)_3Br_2(PPh_3)$ cannot be cleanly produced by wavelength selection. The red-shifted LMCT transitions of $Rh_2(dfpma)_3Br_2(PPh_3)$ tail significantly into the visible spectral region, such that the 436-nm excitation wavelength used to photoconvert $Rh_2(dfpma)_3Br_4$ to $Rh_2(dfpma)_3Br_2(PPh_3)$ is also sufficiently energetic to slowly convert $Rh_2(dfpma)_3Br_2(PPh_3)$, as it is produced, to $Rh_2(dfpma)_3(PPh_3)_2$. Despite this experimental complexity, the PPh_3 system is ideal for quantifying the HBr produced from the overall photoreaction sequence. Although the direct collection of HBr in the headspace above the THF solution is complicated by its small quantities resulting from the low concentration of the $Rh_2(dfpma)_3Br_4$ photoreactant ($\sim$100 μM), HBr may indirectly be detected by its reaction with a nitrogen base. The sterically encumbered 2,6-lutidine proved most useful in our hands, as the methyl groups flanking the amine prevent competitive coordination of the base to the metal center. Bulk photolysis (λ_{exc} > 335 nm, THF, 0 °C) of $Rh_2(dfpma)_3Br_4$ (1 equiv, 20 μmol) was performed in the presence of 2.5 equiv of PPh_3 and 4.3 equiv of 2,6-lutidine, and the ^1H NMR ($CDCl_3$) spectrum of the isolated Rh_2 dfpma and Br photoproducts was recorded. Singlet resonances for the methyl groups of the bridging dfpma ligands of $LRh^0Rh^{II}Br_2$ at 2.83 and 2.91 ppm and of LRh^0Rh^0L at 2.60 and 2.71 ppm distinguish the Rh_2 dfpma photoproducts. A broad singlet at 16.8 ppm and a sharp singlet at 3.02 ppm are signatures of the acid proton and methyl groups, respectively, of lutidinium bromide ($LutH^+Br^-$).[57] Integration of the dfpma methyl proton signals reveals the production of 0.59 equiv of $Rh_2(dfpma)_3Br_2(PPh_3)$ and 0.41 equiv of $Rh_2(dfpma)_3(PPh_3)_2$; the $LutH^+$ resonance integrates to 3.00 equiv. If 2 equiv of HBr is produced for each two-electron photoconversion of $Rh_2(dfpma)_3Br_4$ and $Rh_2(dfpma)_3(PPh_3)_2$, then the production of 1.18 and 1.64 equiv of HBr, respectively, or total of 2.82 equiv of HBr is required to accompany each photolysis reaction. The good agreement between the calculated and experimental yields of $LutH^+Br^-$ establishes Scheme 2 as the overall photoreaction sequence for the Rh_2 dfpma system.

Scheme 2

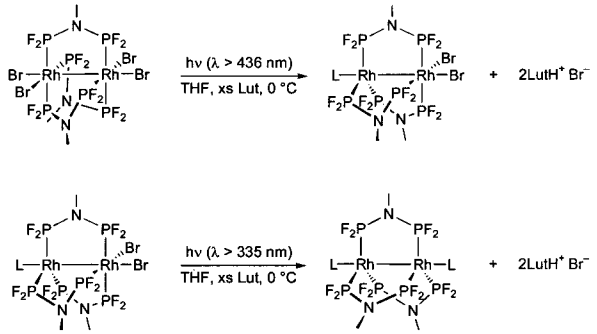

Action Spectra. The product appearance quantum yields (ϕ_p) for the photoreactions of Scheme 2 at selected excitation wavelengths are shown as an overlay on the absorption changes of Figure 6. For $Rh_2(dfpma)_3Br_4$ photochemistry (Figure 6a), ϕ_p values are virtually constant from 313 to 405 nm ($\phi_p^{313-405} = 0.022 \pm 0.003$) but then begin to decrease as λ_{exc} is moved into the visible spectral region ($\phi_p^{436-468} = 0.012 \pm 0.001$). This trend in ϕ_p is in accordance with the spectroscopy of the $Rh_2(dfpma)_3X_4$ series. The ϕ_p values are highest for irradiation wavelengths coincident with the two LMCT absorption bands, where weakening of the Br−Rh−Rh−Br framework results from dσ* population, augmented by depopulation of Rh−X(σ) levels. The reduction in LMCT character in the lower energy absorption band (vide supra) is paralleled by an attenuation in the quantum efficiency as λ_{exc} is moved across the absorption profile. Here, disruption to the Br−Rh−Rh−Br framework is primarily restricted to population of the dσ* orbital, and consequently the framework is more robust under longer wavelength excitation. A similar trend is observed in the action spectrum of $Rh_2(dfpma)_3Br_2(\eta^1\text{-dfpma})$ (Figure 6b), but the onset for the decrease in ϕ_p occurs at shorter wavelengths ($\phi_p^{313-365} = 0.0035(3)$, $\phi_p^{405-436} = 0.0017(3)$). This shift in the action spectrum is consistent with the more reduced $LRh^0-Rh^{II}Br_2$ core (as compared to $Br_2Rh^{II}-Rh^{II}Br_2$), which results in a displacement of the photoactive, metal-reducing LMCT transitions to higher energy. The wavelength shift between the photochemical action spectra of $Rh_2(dfpma)_3Br_4$ and $Rh_2(dfpma)_3Br_2(\eta^1\text{-dfpma})$ is manifest to our ability to deconvolute the photochemical pathways with the wavelength selection experiments of Figure 6.

Electronic Structure Calculations. Molecular orbital calculations emphasize the electronic structure features that are crucial to promoting the four-electron photochemistry of the Rh_2 dfpma series. Figure 7 shows the HOMOs and LUMOs of $Rh_2(dfpma)_3Br_4$, $Rh_2(dfpma)_3Br_2(PF_3)$, and $Rh_2(dfpma)_3(PF_3)_2$ derived from extended Hückel calculations. For each complex, the HOMO is approximately 2-fold degenerate and of metal dδ* or dπ* character, while the LUMO is primarily localized between the metal centers and of σ* character. This homology

(55) Fossey, J.; Lefort, D. *Free Radicals in Organic Chemistry*; Wiley: New York, 1995.

(56) Morse, J. G.; Cohn, K.; Rudolph, R. W.; Parry, R. W. *Inorg. Synth.* **1967**, *10*, 147−159.

(57) Independently prepared lutidinium bromide (formed from the reaction of lutidine with trimethylsilyl bromide and phenol) in $CDCl_3$ exhibits singlet resonances in the ^1H NMR spectrum at 16.3 ppm for the acid proton and at 2.96 ppm for the methyl groups.

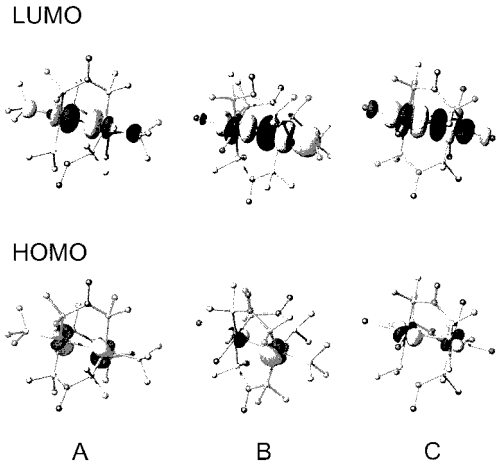

Figure 7. HOMO and LUMO for LRh^0Rh^0L, $LRh^0Rh^{II}Br_2$, and $Br_2Rh^{II}Rh^{II}Br_2$ cores of (A) $Rh_2(dfpma)_3(PF_3)_2$, (B) $Rh_2(dfpma)_3Br_2(PF_3)$, and (C) $Rh_2(dfpma)_3Br_4$, respectively, as determined at the extended Hückel level using YAeHMOP v2.0. For clarity, only metal and bromine orbitals are represented.

of the HOMOs and of the LUMOs is striking, considering the disparate metal coordination geometries and oxidation states across the Rh_2 dfpma series.

The frontier MOs are largely a consequence of the large one-electron splitting arising from the combination of spatially directed d_{z^2} orbitals of the individual fragments composing the Rh_2 dfpma complexes. Consider the Rh^0P_4 (C_{3v}) building block of the $Rh_2(dfpma)_3(PF_3)_2$ complex. The fragment has eight electrons residing in (d_{xz}, d_{yz}) and (d_{xy}, $d_{x^2-y^2}$) orbitals and the odd electron occupying the d_{z^2} orbital.[58] The d_{z^2} orbitals combine to give rise to the dσ* LUMO and a filled dσ level, energetically stabilized relative to the π/π^*(d_{xz}, d_{yz}) and δ/δ^*(d_{xy}, $d_{x^2-y^2}$) manifold. The HOMO is either dδ* or dπ*, with the former prevailing when two Rh^0P_4 fragments are combined. The formal Rh−Rh single bond results from the pairing of the d_{z^2} electrons within the $\sigma(d_{z^2})$ level. Similar orbital energetics are preserved for the $Rh_2(dfpma)_3Br_4$ and $Rh_2(dfpma)_3Br_2(\eta^1\text{-dfpma})_2$ complexes. The $d_{x^2-y^2}$ level of the $Rh^{II}P_3Br_2$ fragment is empty and displaced to high energy owing to the destabilizing $M-L_{eq}$ σ* interactions. Consequently, as with the Rh^0P_4 fragment, the odd electron of the $Rh^{II}P_3Br_2$ fragment resides in the d_{z^2} orbital, with the remaining six electrons of the d^7 metal center occupying the lower energy (d_{xz},d_{yz}) and d_{xy} orbitals. Linear combinations of the $Rh^{II}P_3Br_2$ fragment orbitals with those of another $Rh^{II}P_3Br_2$ fragment to give $Rh_2(dfpma)_3Br_4$, or with those of a Rh^0P_4 fragment to give $Rh_2(dfpma)_3Br_2(\eta^1\text{-dfpma})_2$, lead to a d$\sigma$* LUMO. As was the situation for $Rh_2(dfpma)_3(PF_3)_2$, the dσ level is stabilized significantly with respect to the energetically proximate dπ* and dδ* levels, a result of much smaller one-electron splittings engendered by δ and π overlap. The only difference for the oxidized complexes is that the dπ* orbitals (vs dδ* orbitals of A in Figure 7) emerge as the LUMO. Again, a single Rh−Rh bond arises from electron pairing within the $\sigma(d_{z^2})$ orbital.

As is evident from the pictorial representations of Figure 7, the LUMOs of the oxidized $Br_2Rh^{II}Rh^{II}Br_2$ and $LRh^0Rh^{II}Br_2$ compounds are distinguished from their fully reduced LRh^0Rh^0L counterpart by a $Rh(d_{z^2})-Br(p)\sigma^*$ interaction. Here, the results of the extended Hückel calculation and the observed photochemistry converge. Population of the LUMOs depicted in Figure 7B and C is consistent with Rh−Br bond homolysis as the dominant reaction pathway from electronically excited $Rh_2(dfpma)_3Br_4$ and $Rh_2(dfpma)_3Br_2(\eta^1\text{-dfpma})_2$ complexes. Moreover, a stepwise process for the reductive elimination of bromine is suggested by the nodal structure of the LUMOs. The localization of antibonding character along the metal−metal internuclear axis points toward the initial activation of the Rh−Br_{ax} bond, with Br_{eq} most likely lost in a subsequent elimination step. The intimate mechanistic details of the Br elimination from the Rh^{II} center are currently the focus of ongoing investigations of the transient absorption spectroscopy of Rh_2 dfpma photochemistry.

Conclusions

As one-electron mixed-valence bimetallic cores promote single-electron-transfer reactions, our results show that two-electron mixed-valence bimetallic cores exhibit correspondent two-electron redox chemistry, thus affording a framework in which to rationally design multielectron reactivity. By spanning two-electron reduced LRh^0Rh^0L and two-electron oxidized $X_2Rh^{II}Rh^{II}X_2$ species, the $LRh^0Rh^{II}X_2$ complex sustains the multielectron reactivity of the Rh_2 dfpma system. Photoreactivity is achieved from a dσ* excited state, which transcends state reordering despite a change of four in the formal oxidation state and disparate coordination geometries of the bimetallic core. Our ability to "synthesize" the same reactive excited state across the Rh_2 dfpma series permits us to observe the unprecedented four-electron photoreactivity that we report here.

The Rh_2 dfpma photoredox chemistry extends significantly beyond our previous investigations of two-electron mixed valency by allowing us to develop the approach within electronic structure constructs that are more typical of inorganic metal complexes. In our studies of the photochemistry of multiply bonded metal−metal complexes, excitation of the lowest energy metal-localized transitions produces two electrons that are effectively paired in an orbital localized at one center of the bimetallic core (with a corresponding two-electron hole at the other center).[59] The resultant $M^+-M:^-$ zwitterion is the suspected intermediary of two-electron addition reactions to electronically excited quadruply bonded metal−metal dimers[60] and of two-electron elimination reactions from electronically excited, multiply bonded edge-sharing bioctahedral complexes.[61] Although conceptually appealing, this valence bond approach is difficult to generalize because the excited states of *most* binuclear complexes are derived from the population of molecular orbitals that are *delocalized* over the entire bimetallic core. In the Rh_2 dfpma chemistry, the two-electron mixed-valence character is built directly into the ground state of the $LRh^0Rh^{II}X_2$ complex. Absorption of a photon produces a more energetic excited state that is predisposed to react in two-electron steps at the individual metal centers of an electronically delocalized bimetallic core. This strategy is generally applicable to any other bimetallic core featuring lowest energy electronic

(58) Albright, T. A.; Burdett, J. K.; Whangbo, M.-H. *Orbital Interactions in Chemistry*; Wiley-Interscience: New York, 1985.

(59) (a) Engebretson, D. S.; Zaleski, J. M.; Leroi, G. E.; Nocera, D. G. *Science* **1994**, *265*, 759−762. (b) Engebretson, D. S.; Graj, E. M.; Leroi, G. E.; Nocera, D. G. *J. Am. Chem. Soc.* **1999**, *121*, 868−869.

(60) (a) Hsu, T.-L. C.; Helvoigt, S. A.; Partigianoni, C. M.; Turró, C.; Nocera, D. G. *Inorg. Chem.* **1995**, *34*, 6186−6190. (b) Hsu, T.-L. C.; Engebretson, D. S.; Nocera, D. G. *Inorg. Chim. Acta* **1995**, *240*, 551−557. (c) Hsu, T.-L. C.; Chang, I.-J.; Ward, D. L.; Nocera, D. G. *Inorg. Chem.* **1994**, *33*, 2932−2937. (d) Partigianoni, C. M.; Turró, C.; Hsu, T.-L. C.; Chang, I.-J.; Nocera, D. G. In *Photosensitive Metal-Organic Systems*; Kutal, C., Serpone, N., Eds.; ACS Advances in Chemistry Series 238; American Chemical Society: Washington, DC, 1993; pp 147−163. (e) Partigianoni, C. M.; Nocera, D. G. *Inorg. Chem.* **1990**, *29*, 2033−2034.

(61) Pistorio, B. J.; Nocera, D. G., submitted for publication.

excited states resulting from strongly coupled metal centers as long as a two-electron mixed-valence complex can be stabilized with respect to its symmetric congener.

The Rh_2 dfpma system circumvents problems previously associated with the utilization of two-electron mixed valency in the design of multielectron schemes. Prior to the studies described here, the presence of a two-electron mixed-valence intermediate has been observed to render complexes inert to further oxidation−reduction chemistry.[62−64] This redox deactivation has been attributed to the inability of the coordination sphere to electronically and conformationally support the appropriate energetics that make the bimetallic core amenable to further reaction.[65] Along this line, the redox cooperativity of the $LRh^0Rh^{II}X_2$ dfpma complex appears to be derived from the ligand framework. The flexibility of the dfpma ligand allows for the respective octahedral and trigonal bipyramidal geometries of di- and zerovalent rhodium to be accommodated with facility. Moreover, as demonstrated by the crystal structure of $Rh_2(dfpma)_3Br_2(PPh_3)$, the ligand's unique electronic properties enable the stabilization of metals in both the high and low formal oxidation states required for the overall multielectron reactivity of Scheme 2. A recent study similarly exploits redox cooperativity of a diiron core within a flexible carboxylate coordination environment to drive the two-electron reduction of oxygen to peroxide, presumably through a one-electron mixed-valence intermediate.[66] In the dfpma chemistry, the ability to support a two-electron mixed-valence core allows redox cooperativity of the bimetallic core to be achieved in the sum of four electrons. The emergence of such reactions along ground-state and excited-state pathways suggests that redox cooperativity within mixed-valence bimetallic cores will be a useful design concept in the future development of multielectron reaction schemes.

Coupled two-electron photoreactions assume a prominent status in energy conversion chemistry, especially when a metal−halide bond is involved. Consider the splitting of hydrohalic acids to H_2 and X_2. Irrespective of practical concerns, the achievement of HX splitting chemistry would represent a prodigious accomplishment, as it requires a metal photocatalyst to harness a photon to drive a multielectron redox event that is thermodynamically unfavorable from the ground state. Whereas the elimination of H_2 from metal centers is feasible, the benchmark studies on the energy conversion chemistry of $d^8\cdots d^8$ dimers over the past two decades show that the elimination of X_2 poses a more significant challenge owing to the high stabilities of the metal−halide bond.[25,67] For instance, the HX photochemistry of Rh^IRh^I diisocyanide complexes is stoichiometric because the cycle to regenerate the initial photoreagent terminates with the formation of the Rh^{II}−X bond.[25,68] The incorporation of a dσ* excited state across the $Rh_2(dfpma)_3Br_4$, $Rh_2(dfpma)_3Br_2L$, $Rh_2(dfpma)_3L_2$ series allows us to overcome the energetic barrier to halogen atom elimination, and therefore provides a means for interconversion between the series members in two-electron steps. Current investigations are exploring whether we can maintain a related four-electron photochemistry for the Rh_2 dfpma (and kindred ligand) series when X_2 is replaced by HX.

Acknowledgment. The authors thank Dr. Aaron Odom for stimulating discussions and Dr. William M. Davis for assistance with the solution of the X-ray crystal structures. The National Science Foundation (Grant CHE-9817851) funded this research.

Supporting Information Available: Input files for YAeHMOP calculations, and ORTEP representations, tables of crystal data, atomic coordinates, bond lengths and angles, anisotropic thermal parameters, and hydrogen coordinates for $Rh_2(dfpma)_3(\eta^1\text{-dfpma})_2$ and $Rh_2(dfpma)_3Br_2(PPh_3)\cdot 1.5CH_2Cl_2$ (PDF). An X-ray crystallographic file, in CIF format, is available through the Internet only. This material is available free of charge via the Internet at http://pubs.acs.org.

JA9902017

(62) (a) Halpern, J. *Inorg. Chim. Acta* **1982**, *62*, 31−37. (b) Halpern, J.; Goodall, B. L.; Khare, G. P.; Lim, H. S.; Pluth, J. J. *J. Am. Chem. Soc.* **1975**, *97*, 2301−2303. (c) Halpern, J.; Wong, C. S. *Chem. Commun.* **1973**, 629−630.

(63) (a) Schenck, T. G.; Downes, J. M.; Milne, C. R. C.; Mackenzie, P. B.; Boucher, H.; Whelan, J.; Bosnich, B. *Inorg. Chem.* **1985**, *24*, 2334−2337. (b) Schenck, T. G.; Milne, C. R. C.; Sawyer, J. F.; Bosnich, B. *Inorg. Chem.* **1985**, *24*, 2338−2344. (c) Bosnich, B.; Boucher, H.; Marshall, C. *Inorg. Chem.* **1976**, *16*, 634−638.

(64) Tolman, C. A.; Meakin, P. Z.; Lindner, D. L.; Jesson, J. P. *J. Am. Chem. Soc.* **1974**, *96*, 2762−2774.

(65) McCollum, D. G.; Bosnich, B. *Inorg. Chim. Acta* **1998**, *270*, 13−19.

(66) Mizoguchi, T. J.; Lippard, S. L. *J. Am. Chem. Soc.* **1998**, *120*, 11022−11023.

(67) Marshall, J. L.; Steigman, A. E.; Gray, H. B. In *Excited States and Reactive Intermediates*; Lever, A. B. P., Ed.; ACS Symposium Series 307; American Chemical Society: Washington, DC, 1986; pp 166−176.

(68) Gray, H. B.; Maverick, A. W. *Science* **1981**, *214*, 1201−1205.